

Simple Artificial Neuron Using an Ovonic Threshold Switch Featuring Spike-Frequency Adaptation and Chaotic Activity


Milim Lee,^{1,2} Seong Won Cho,^{1,3} Seon Jeong Kim,^{1,3} Joon Young Kwak,¹ Hyunsu Ju,⁴ Yeonjin Yi,² Byung-ki Cheong,¹ and Suyoun Lee^{1,3,*}

¹Center for Electronic Materials, Korea Institute of Science and Technology, Seoul 02792, Korea

²Institute of Physics and Applied Physics, Yonsei University, Seoul 03722, Korea

³Division of Nano & Information Technology, Korea University of Science and Technology, Daejeon 34316, Korea

⁴Center for Opto-Electronic Materials and Devices, Korea Institute of Science and Technology, Seoul 02792, Korea

 (Received 18 March 2020; revised manuscript received 8 May 2020; accepted 26 May 2020; published 23 June 2020)

As an essential building block for developing a large-scale brain-inspired computing system, we propose a highly scalable and energy-efficient artificial neuron device composed of an ovonic threshold switch (OTS) and a few passive electrical components. It is found that the proposed neuron device shows not only the basic integrate-and-fire function and the rate-coding property, but also the spike-frequency-adaptation (SFA) property and the chaotic activity of biological neurons, the most common features found in mammalian cortex, but they have been hard to achieve up to now. In addition, it is shown that the energy consumption of the OTS-based neuron device scales with the size of the OTS device, extrapolating both the size and the energy efficiency to the level of a biological neuron in a human brain with state-of-the-art technology. Finally, using the OTS-based neuron device combined with the reservoir computing technique, the spoken-digit recognition task has been performed with a considerable degree of recognition accuracy (94%). These results demonstrate that our OTS-based artificial neuron device is promising for the application in the development of a large-scale brain-inspired computing system.

DOI: [10.1103/PhysRevApplied.13.064056](https://doi.org/10.1103/PhysRevApplied.13.064056)

I. INTRODUCTION

Brain-inspired computing systems have attracted much interest because of the outstanding energy efficiency of the human brain, however, these have been unachievable using traditional computing systems adopting the von Neumann architecture [1]. As a building block, neuron-mimicking devices based on Si-MOSFETs have been introduced [2–5], but the scalability and the energy efficiency of those devices are still problematic to apply in a large-scale computing system since they require tens of n -MOSFETs and p -MOSFETs to compose a single neuron device.

As a solution to this problem, we suggest a simple artificial neuron device based on the ovonic threshold switch (OTS). The composite artificial neuron device used in this experiment is schematically presented in Fig. 1(a), which is composed of an OTS, two resistors (R_1 and R_2), and a capacitor (C). An OTS device has metal–amorphous-chalcogenide–metal structure, which was reported to show a reversible electrical switching by Ovshinsky in 1968 [6–15]. Due to its superior switching characteristics such

as high on:off ratio ($>10^4$) and high current capacity ($>10^6$ A/cm²), it is currently utilized as a selector device in a commercial high-density nonvolatile memory device (Optane™, Intel) [16,17].

Based on the characteristic threshold switching of the OTS device [see the inset of Fig. 1(a)], the oscillating behavior of the supposed artificial neuron can be easily understood. As a voltage signal enters V_{in} with amplitude higher than V_{th} of the OTS, as long as the OTS is in its *off* state, the capacitor C is charged up leading to a gradual increase in V_{mem} , similar to the integration phase of a biological neuron. When V_{mem} reaches V_{th} , the resistance of the OTS decreases drastically resulting in the generation of a spike current (I_S) through the OTS and R_2 , similar to the firing of a biological neuron. As a result, C is discharged and V_{mem} decreases. When V_{mem} decreases down to V_H of the OTS, the OTS is turned off and C starts to be charged up again completing one cycle of oscillation [see Fig. 1(b)]. A similar nonlinear oscillator was first reported by Pearson and Anson in 1922 [18,19], where the OTS in Fig. 1(a) was replaced with a neon lamp. In addition, with a phase-change memory device instead of the OTS, such a relaxation-oscillating behavior was demonstrated [20,21].

*slee_eels@kist.re.kr

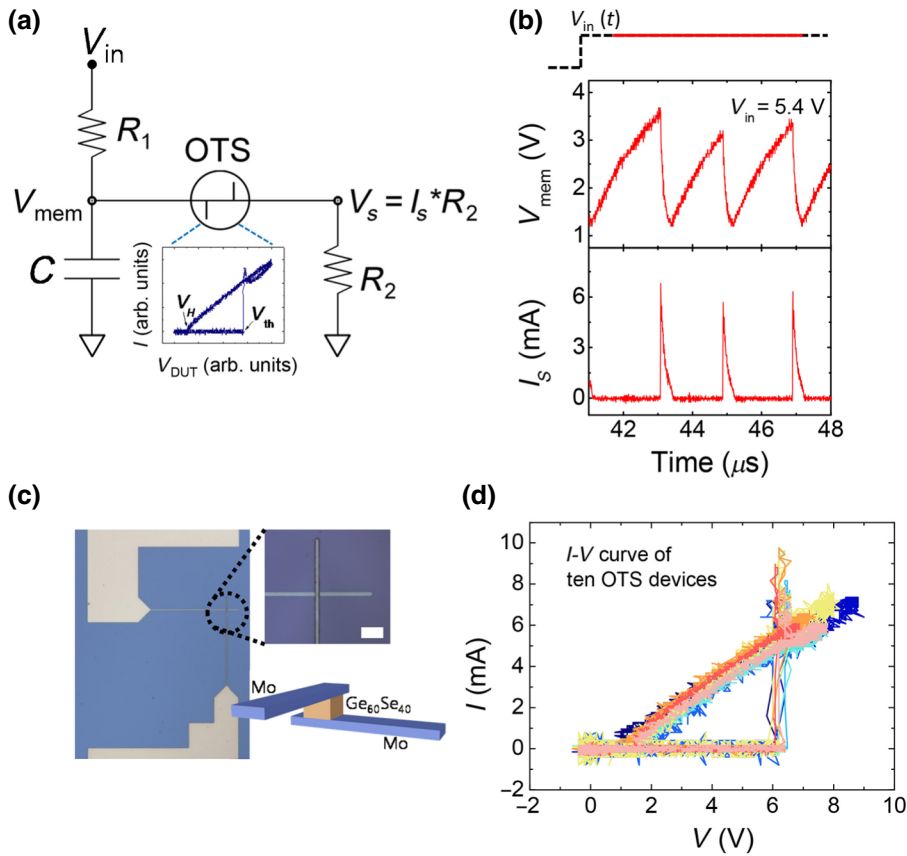


FIG. 1. Artificial neuron based on OTS (a) An artificial neuron circuit composed of two resistors (R_1 and R_2), one capacitor (C), and one OTS device. V_{mem} and I_s represent the membrane potential and the spike current, respectively. (Inset) Characteristic $I-V$ curve of an OTS device. (b) Integrate-and-fire behavior: $V_{mem}(t)$ (upper panel) and $I_s(t)$ (lower panel) of a device as a response to a dc voltage input ($V_{in}=5.4$ V). (c) Optical microscope image of an OTS device, which has a crosspoint sandwich structure (scale bar = 20 μm). (d) Pulsed current-voltage ($I-V$) characteristic curves of ten OTS devices.

Recently, artificial neuron devices have been introduced, which are based on functional materials, for example, phase-change materials [22] and Mott insulators [23–25]. And very recently, it has been reported that plural behaviors of biological neurons can be plausibly mimicked by a device composed of two VO_2 -based switching devices and several passive electrical elements [26]. However, there is a problem yet to be solved, which is the operation temperature limited by the phase-transition temperature. The relatively low transition temperature of VO_2 (approximately 67 $^{\circ}C$) [27] casts doubt on its practicality as pointed out by the authors. One solution may be to increase the transition temperature by doping some elements but with an expense of increase in the energy consumption. In this regard, a solution can be to use the OTS device, where the electrical switching is described by the trap-mediated excitation of carriers followed by an avalanche [12,13], which is very different from that of the Mott insulator. Furthermore, the OTS is compatible with a CMOS process as proved by the application in commercial devices, another important requirement for the application. In this work, we investigate the behaviors of the proposed neuron device to find that it shows integrate-and-fire (IF) and rate-coding behavior, two basic requirements of a neuron-mimicking device. Furthermore, the spike-frequency adaptation (SFA) and chaotic activity are observed in our device, which are the most common features found in the

mammalian cortex [28] and are crucial keys to implementing energy-efficient signal processing, learning, and adaptation to environments [29–31].

II. EXPERIMENTS

In Fig. 1(c), an optical microscope image and a schematic illustration of the cross-point structured OTS device are shown. In this work, $Ge_{60}Se_{40}$ is used as an active switching material, which is sandwiched in between Mo electrodes [32]. OTS devices are fabricated with a cross-point structure composed of metal(bottom electrode, Mo 100 nm)/ $Ge_{60}Se_{40}$ (100 nm)/metal(top electrode, Mo 100 nm) using photolithography and lift-off techniques. $Ge_{60}Se_{40}$ thin films are deposited by co-sputtering technique using Ge and $Ge_{40}Se_{60}$ targets. The composition of $Ge_{60}Se_{40}$ film is analyzed using electron probe micro analysis (EPMA) and x-ray fluorescence (XRF) technique. The electrode (Mo) films are deposited by rf sputtering technique as well. Such fabricated OTS devices show uniform switching behavior as can be found in Fig. 1(d).

The composite artificial neuron devices are composed of an OTS device, commercial resistors, and a commercial capacitor. The device characteristics are investigated by applying a stimulus to V_{in} in Fig. 1(a) (voltage pulse, Agilent 81110A and Tektronix AFG-3101) and measuring V_{mem} and I_s simultaneously (Tektronix TDS-5104). We

investigate dozens of devices with varying the size of the OTS device, R_1 , R_2 , and C .

III. RESULTS AND DISCUSSION

A. Integrate-and-fire and rate coding

Figure 1(b) shows the aforementioned gradual increase in $V_{\text{mem}}(t)$ and the generation of $I_S(t)$ in our composite device ($R_1=10\text{ k}\Omega$, $C=10\text{ pF}$, $R_2=100\text{ }\Omega$), which is driven by a dc voltage (5.4 V) at V_{in} . This unequivocally implies that our composite device can mimic the IF behavior of a biological neuron. In addition, we investigate the response of our OTS-based neuron device with varying amplitude of the input voltage in the range of 5.4 ~ 7.0 V. In Fig. 2(a), the average firing rate clearly increases corresponding to the incremental input voltage. To further clarify the change, the spectral density of $I_S(t)$ is plotted as a function of frequency in Fig. 2(b). It apparently shows that the peak position of the spectral density shifts toward the higher frequency. This behavior is consistent with the “rate coding” of a biological neuron [33] supporting the feasibility of our composite device as an artificial neuron device.

B. Spike-frequency adaptation

In the mammalian neocortex, the excitatory neurons show a gradual elongation of the interval between spikes for a constant stimulus, which is called SFA. It is valued as a critical role to enable the energy-efficient signal processing in brains [4,28]. It is intriguing to find that spike patterns in Fig. 2(a) show the SFA-like behavior; for example, $I_S(t)$ for $V_{\text{in}}=7.0\text{ V}$ shows the behavior well. The observed spike pattern shows a repetition of a reset followed by the SFA, which is rather different from the pure SFA behavior. We consistently observe such a SFA-like behavior in tens of our neuron devices.

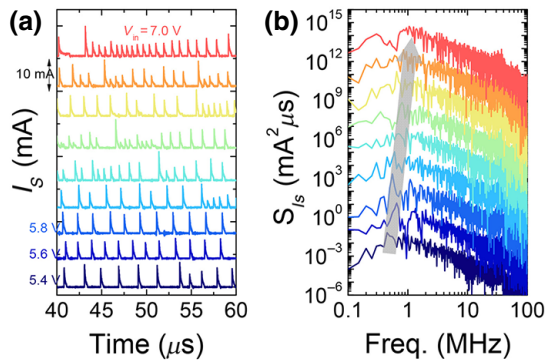


FIG. 2. Rate coding (a) $I_S(t)$ as a response to various voltage inputs (5.4–7 V, 0.2 V step). (b) Spectral density of I_S (S_{I_S}) for the input voltages the same as (a). Curves in (a) and (b) are shifted vertically for clarity.

As a representative example, a small region of $V_{\text{mem}}(t)$ and $I_S(t)$ for $V_{\text{in}}=6.2\text{ V}$ in Fig. 2(a) is expanded in Fig. 3(a), which shows two sets of sequential spikes featuring the aforementioned SFA behavior. In Fig. 3(b), the latter set of spikes (after 50 μs) is expanded, clearly showing the gradual increase in interspike interval (ISI) with the spike count. To be more quantitative, the firing rate [$f_{\text{spike}}(t)$] for $I_S(t)$ for $V_{\text{in}}=7.0\text{ V}$ in Fig. 2(a) is plotted as a function of the time in Fig. 3(c), where $f_{\text{spike}}(t)$ is defined as the reciprocal of ISI. It is found that $f_{\text{spike}}(t)$ is well described by an exponential decay represented as a red solid line in Fig. 3(c) [$f_{\text{spike}}(t)=f_{\text{offset}}+f_1\exp(-t/t_0)$, where f_{offset} , f_1 , and t_0 are constants]. Such an exponential decay of $f_{\text{spike}}(t)$ closely resembles the SFA behavior of biological neurons [5,34,35].

As for the origin of the SFA behavior in our neuron device, we suggest a model described in Figs. 3(d)–3(i) [together with Fig. 3(b)], where the sequential changes in V_{th} are related with those in the filling of the trap states in the OTS. In line with what was mentioned above, the electrical switching in the OTS device is described by the trap-mediated excitation of carriers followed by an avalanche [12,13]. Let us assume that, in Fig. 3(d), a voltage bias ($-V_{\text{bias}} < 0$) is applied to the left electrode (source) with the right one (drain) being grounded. The shaded region represents the filled trap states. When $V_{\text{bias}}=V_{\text{th}}$, the highest filled trap states come across the edge of the conduction band of the chalcogenide near the drain and the carriers in the trap states become free, turning the chalcogenide material into conductive [Fig. 3(e)]. As a result, the width of the *off* region is reduced leading to the increase in the electric field over the remaining *off* region, which accelerates the reduction of the *off* layer width. In this manner, the *off* region vanishes abruptly and large current flows through the device instantly [Fig. 3(f)]. As V_{bias} decreases below V_H , the trap states start to be evacuated below the edge of the conduction band by the emission of carriers, leading to the formation of the *off* layer. However, the formation of the *off* layer proceeds much more slowly compared to the switch-on process due to the slow evacuation process in the weak applied field and, as a result, it is expected that a hill-like distribution of the filled trap states is formed as shown in Fig. 3(g). In this state, the device is in its *off* state but the effective *off* layer is thinner than the initial *off* state resulting in the lower V_{th} ($V_{\text{th}1}$) compared to the initial V_{th} ($V_{\text{th}0}$). As V_{OTS} increases again by charging and reaches up to $V_{\text{th}1}$, the OTS is turned on again [Fig. 3(h)] but the current is lower than the first *on* state because of the low bias voltage. The lower current level implies that the trap states are less filled compared to Fig. 3(f) and that, after a certain discharging period, there will be more empty trap states than in Fig. 3(g). Therefore, the *off*-layer width increases as shown in Fig. 3(i) leading to the higher V_{th} ($V_{\text{th}2}$) compared to $V_{\text{th}1}$. This picture explains the SFA property observed in our device in a way

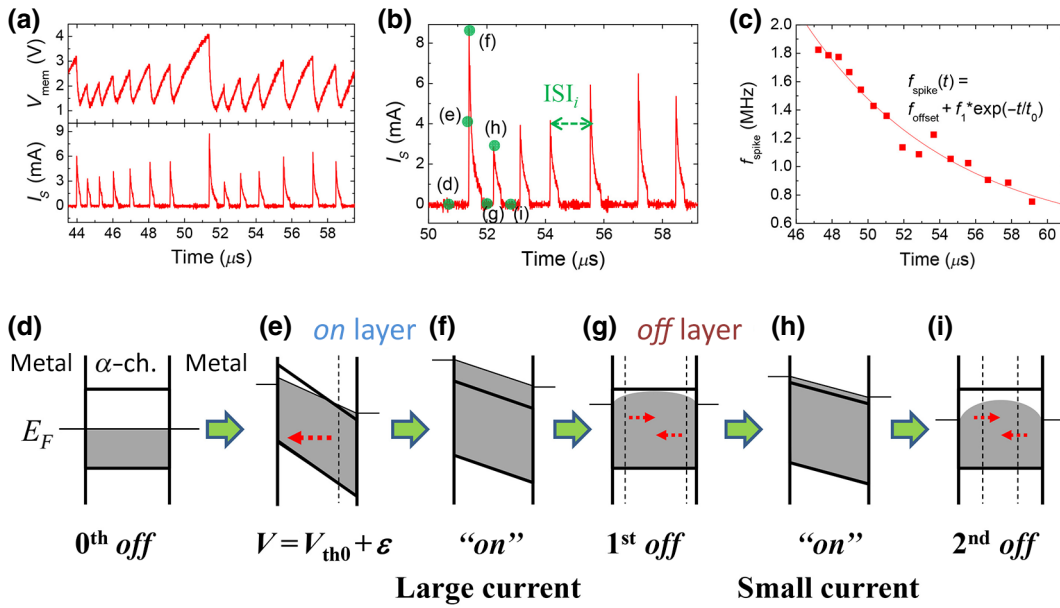


FIG. 3. Spike-frequency adaptation (a) $V_{\text{mem}}(t)$ and $I_S(t)$ for $V_{\text{in}} = 6.2$ V in Fig. 2(a). (b) Magnified view of (a) in the range from 50 to 59 μs , where (d)–(i) correspond to the following figures (d)–(i), which explains a model suggested in this work (see the main text). ISI represents the interspike interval between adjacent spikes. (c) Firing rate (f_{spike}) as a function of time. The red solid line is a fitting curve modeled by the simple exponential decay $f_{\text{spike}}(t) = f_{\text{offset}} + f_1 \exp(-t/t_0)$. (d)–(i) A sequential change in V_{th} due to the change in the filling of trap states after switching, where the shaded region represents the filled trap states. Black dashed lines represent the virtual boundary of the *off* layer or the *on* layer, which is imagined to move along the red dotted arrows whose length represents the speed.

consistent with sequential change in the amplitude of $I_S(t)$ shown in Fig. 3(b).

The validity of the suggested model can be tested by investigating the spike-count dependence of the capacitance of the OTS device, which depends on the width of the *off* layer. However, from an analysis of the time constants during the charging and discharging periods, we find that the capacitance of the OTS device is dominated by a parasitic capacitance making an analysis of the change in capacitance hardly meaningful (see Sec. S1 within the Supplemental Material [36–38]). As an alternative to the capacitance, the delay time (t_d), a quiescent duration for the onset of switching after the application of a super-threshold voltage to an OTS device [see Fig. S2(b) within the Supplemental Material [38]], provides information about the trap states [39,40]. For the OTS device under an electrical bias, an electron residing in trap states is supposed to move by a thermally assisted hopping process and be able to reach a critical energy level for switching after a lot of inelastic hopping processes. In this picture, t_d is interpreted as the total elapsed time during the hopping processes up to the point of switching, and thus it depends on the density of empty trap states and the electric field, the latter of which is inversely proportional to the *off*-layer width. Therefore, the dependence of t_d on the switching count can provide information about the change of the

off-layer width with the switching count. To this end, we perform a test where ten consecutive pulses are applied to an OTS device with a super-threshold voltage and t_d is measured as a function of the switching count (see Sec. S2 within the Supplemental Material [38,39]). Although t_d shows a large variation over different sets of measurements at each switching count because of the stochastic nature of the capture and emission process, it has been clearly observed that t_d tends to increase with the switching count supporting the suggested model.

As another possibility, the change in the temperature inside the OTS is conceivable in that V_{th} of an OTS is known to decrease with increasing temperature [39,41–43]. In this vein, from Fig. 2(a), it is noticed that the firing V_{mem} has the minimum next to the big spike and gradually increases, which may be construed as being due to a temperature rise from Joule heating after the first big spike followed by a slow decay. Such a change in temperature with time may ostensibly explain the observed evolution of V_{th} with time. Nevertheless, the increase in the temperature is estimated to be at most 10 K using the specific heat of GeSe (approximately 20 J/g K) [44], the density (approximately 5 g/cm³) of GeSe, the geometry of the device (area = 25 μm^2 , thickness = 100 nm), and the energy consumption per spike (approximately 1 nJ/spike). Therefore, the increase in the temperature by Joule heating

is too small to explain the observed drastic reduction in V_{th} after the big spike.

C. Chaotic activity

In Fig. 2(a), it is found that $I_S(t)$ is represented by a mixture of the SFA-featured spikes and irregular spikes. From measurements of tens of our neuron devices, we usually observe such a behavior although the relative strengths of the SFA-featured and irregular spikes are varied depending on the values of C , R_1 , and R_2 . To investigate the nature of the irregular spikes, we firstly check if they are of chaotic nature as in the case of a biological neuron [29]. By a chaotic system, it means a system whose state variables are expressed in terms of coupled first-order nonlinear differential equations [45]. That is to say, it is a deterministic nonlinear dynamic system whose state variables evolve in time with a strong dependence on the initial conditions. In a single neuron and neural networks, it is known that the chaotic activity is a key ingredient in realizing adaptability and analog computation in brains [30,46,47]. Recently, it was demonstrated through simulations that a few examples of complex problems related to the global optimization can be solved efficiently by using an array of chaotic neuron devices [25].

For our devices, where the OTS serves as a variable resistor with its resistance depending on both the bias voltage and its history, it is found that the equations describing

the dynamics of our composite neuron device are consistent with the aforementioned definition of a chaotic system (see Sec. S3 within the Supplemental Material [38]). Apart from the mathematical definition, the experimental evidences of the chaotic nature are as follows. In Fig. 4(a), a power-density spectrum ($S_{V_{mem}}$) is presented, which is obtained by fast Fourier transform (FFT) of $V_{mem}(t)$ of a composite neuron with $C=2$ pF, $R_1=5$ k Ω , and $R_2=100$ Ω sampled at a rate of 65 MHz. It shows a broad peak around 0.3 MHz followed by a slow decay, which is described by $S_{V_{mem}} \sim f^{-\nu}$ with $\nu \sim 3.5$. The shape of the observed spectral dependence is quite similar to that of a squid giant axon [48,49], although the frequency range is much higher (approximately 10^4 times) and the slope of the decay is a little steeper in our device compared to those of a squid giant axon ($f_{max} \sim 10$ Hz, $\nu = 1-3$).

As a typical test of a chaotic behavior of a state variable $x(t)$ of an unknown system, the time-delay embedding plot test [45] is useful, which is a plot of the trajectory of $[x(t), x(t+\Delta t), \dots, x(t+n\Delta t)]$ with Δt being a delay time. For a chaotic system, the trajectory forms a confined band called an attractor and the distance between neighboring points in the attractor increases with time due to the nonlinear nature of it. In Fig. 4(b), the time-delay embedding plot of $[I_S(t), I_S(t+\Delta t), I_S(t+2\Delta t)]$ ($\Delta t=32$ nsec) is plotted, clearly showing that the trajectory resides within a band. The type of attractor shown in Fig. 4(b) is called a strange attractor

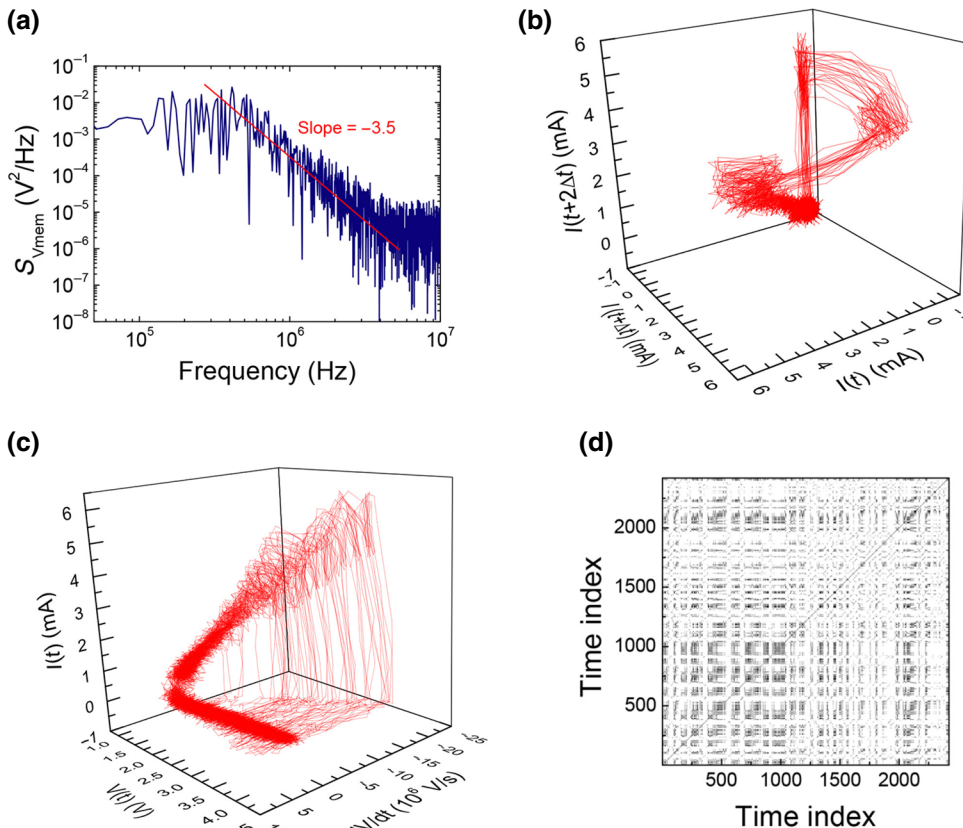


FIG. 4. Chaotic activity. (a) Spectral density of V_{mem} ($S_{V_{mem}}$) of the artificial neuron obtained by fast Fourier transform, where $C=2$ pF, $R_1=5$ k Ω , $R_2=100$ Ω . (b) Time-delay embedding plot (trajectory of $[I_S(t), I_S(t+\Delta t), I_S(t+2\Delta t)]$) ($\Delta t=32$ nsec) showing a strange attractor characterizing a chaotic system. (c) Trajectory of $[I_S(t), V_{mem}(t), dV_{mem}(t)/dt]$ showing a similar trajectory of a biological neuron. (d) A recurrence plot of $V_{mem}(t)$, where the value at time indices (i, j) is unity only if the difference between $V_{mem}(i)$ and $V_{mem}(j)$ is smaller than a threshold or zero otherwise, showing that the three relaxed conditions of Devaney's chaos are shown to be satisfied (black and white dots represent unity and zero, respectively).

[45], which is widely observed in biological neurons [50–54]. In Fig. 4(c), a trajectory of $[I_S(t), V_{\text{mem}}(t), dV_{\text{mem}}(t)/dt]$ is also plotted, which has been studied considerably in various biological neurons such as Onchidium pacemaker neuron [51] and squid giant axon [52,53]. It is found that $[V_{\text{mem}}(t), dV_{\text{mem}}(t)/dt]$ of our device shows a structure of beaks and wings, which is similar to that of biological neurons [52–54].

As a final check of the chaotic activity and the similarity between biological neurons and our device, a recurrence plot [55,56] is presented in Fig. 4(d) where the value at a position in phase space of time indices (i, j) is unity only if the difference between $V_{\text{mem}}(i)$ and $V_{\text{mem}}(j)$ is smaller than a certain threshold, which depends on the system under investigation, or zero otherwise. The recurrence plot obtained with the threshold of 0.7 mV, shown in Fig. 4(d), is found to satisfy the three relaxed conditions of Devaney's chaos [57–59] apparently indicating that our device is a chaotic system. Furthermore, it is found that the recurrence plot is quite similar to that of the squid giant axon [59], strongly supporting the similarity of the chaotic activity of our neuron device to that of biological neurons.

D. Energy consumption

In Fig. 5(a), $V_{\text{mem}}(t)$, $I_S(t)$, and the calculated power $P(t) = V_{\text{mem}}(t) * I_S(t)$ of an OTS-based neuron are plotted as a function of time, giving the energy consumption per spike (E_{sp}) around 1.2 nJ/spike. It is much larger compared to neuron devices based on Si-MOSFETs (1–100 pJ/spike) and a biological neuron (1–10 fJ/spike), which is attributed to the large size of our OTS device resulting in a large *on* current (approximately mA). As a proof-of-concept demonstration is the primary purpose of this work, we use the μm -sized OTS device in this work. In real applications, a sub- μm -scale OTS device will be used resulting in a much lower *on* current. To assess the energy scalability, we investigate E_{sp} of dozens of neuron devices with various sized OTS device to find a power-law relationship ($E_{\text{sp}} \sim S^{0.8}$) between E_{sp} and the size of the OTS device (S) [see Fig. 5(b)]. By extrapolating the trend, it is found that the OTS-based neuron device can achieve the energy efficiency (EE) of a biological neuron in a human brain at the OTS size of 10×10 (nm²) and the thickness of 10 nm, which is expected to be achievable in the near future [60].

Another viable route to reduce E_{sp} is found through the optimization of the device parameters (R_1 , C , and R_2). It is found that the behaviors of the OTS-based neuron sensitively depend on the device parameters, which can be explained by a simple circuit model (see Sec. S4 within the Supplemental Material [38]). Using a SPICE (simulation program with integrated circuit emphasis) model where the OTS is modeled as a parallel connection between a voltage-controlled switch and a capacitor (C_{OTS}) (see

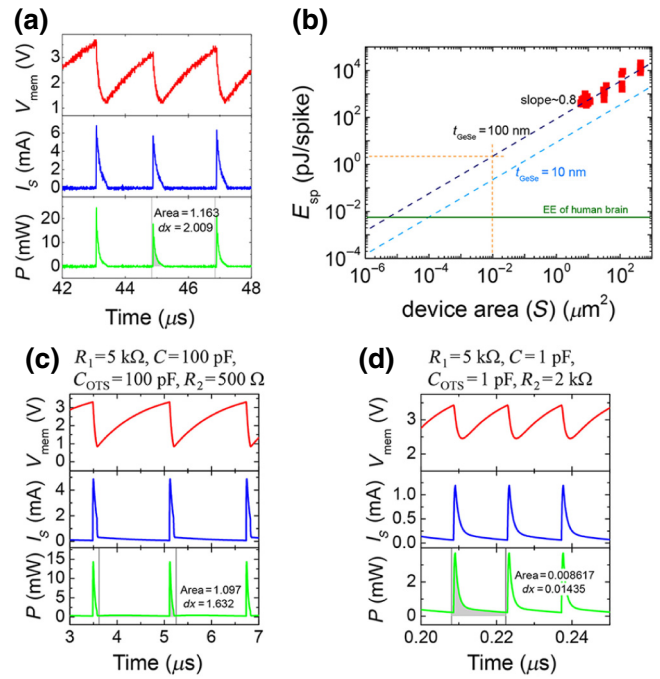


FIG. 5. Energy consumption (a) V_{mem} (top), I_S (middle), power (bottom) of an OTS-based neuron device. In the bottom panel, the energy consumption per spike can be obtained from the area below the curve leading to about 1.2 nJ/spike. (b) Energy scalability of the OTS-based neuron device. (c), (d) Simulated V_{mem} (top), I_S (middle), power (bottom) of a model OTS-based neuron device with $[R_1, C, C_{\text{OTS}}, R_2] = [5 \text{ k}\Omega, 100 \text{ pF}, 100 \text{ pF}, 0.5 \text{ k}\Omega]$ (c) and $[5 \text{ k}\Omega, 1 \text{ pF}, 1 \text{ pF}, 2 \text{ k}\Omega]$ (d), respectively.

Fig. S5 within the Supplemental Material [38]), we examine the effect of the device parameters on E_{sp} to find that E_{sp} is proportional to $C + C_{\text{OTS}}$. Figure 5(c) shows a simulated result for a model device with $[R_1, C, C_{\text{OTS}}, R_2] = [5 \text{ k}\Omega, 100 \text{ pF}, 100 \text{ pF}, 0.5 \text{ k}\Omega]$, which is very similar to Fig. 5(a). On the other hand, Fig. 5(d) shows a result for a model device with $[5 \text{ k}\Omega, 1 \text{ pF}, 1 \text{ pF}, 2 \text{ k}\Omega]$ whose energy consumption is less than 1% of that shown in Fig. 5(c). Indeed, the capacitance around 100 pF is not realistic in sub- μm -scale devices, implying that it originates from the parasitic capacitance, for example, capacitance between lead lines, pads, and/or substrate. Therefore, the above results indicate that the OTS-based neuron device is a promising candidate building block for a large-scale brain-inspired computing system.

E. Demonstration of application feasibility: spoken-digit recognition

To demonstrate the feasibility of our OTS-based neuron device as applied to real neuromorphic devices, we implement a benchmark test of spoken-digit recognition using a reservoir computing technique combined with delayed feedback dynamics [61–63]. In this technique, a single neuron device can emulate a complex neural network by

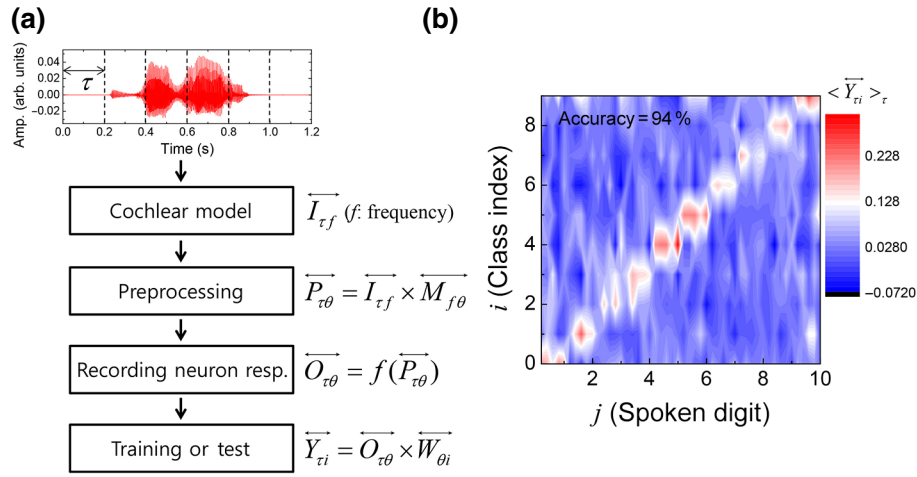


FIG. 6. Spoken-digit recognition. (a) Schematic flowchart for spoken-digit recognition, which is composed of four steps: (1) obtaining frequency components according to the cochlear model, (2) preprocessing procedure through which the frequency components are mapped to virtual nodes (virtual neurons), where $M_{f\theta}$ is a masking matrix, (3) recording neuron response to the input $P_{\tau\theta}$, and (4) training for calculating the optimum synaptic weight $W_{\theta i}$, where i is a class index (0–9, integer). As for the test in step (4), the pre-trained $W_{\theta i}$ is used for calculating $Y_{\tau i}$, whose average over τ 's, $\langle Y_{\tau i} \rangle_{\tau}$ gives the guessed digit for the maximum $\langle Y_{\tau i} \rangle_{\tau}$. (b) A colormap of $\langle Y_{\tau i} \rangle_{\tau}$ as a function of the input spoken-digit ($j = 0-9$, integer) and the class index (i), where the j values are horizontally shifted in order to distinguish the same digits from different speakers (see the text). The best recognition accuracy of 94% is obtained.

taking advantage of time-multiplexing technique. For the test, we use a subset of the TI-46 database [62,64], which consists of 500 spoken-digit voice files taken from ten utterances of five females (10 digits \times 10 utterances \times 5 females = 500 voice files).

In Fig. 6(a), a schematic flowchart is shown for the spoken-digit recognition, which consists of four steps. In the first step, an input voice waveform is divided into N_{τ} sections, which has been set to five in this work. Each section is analyzed to give amplitudes corresponding to frequency channels ($N_f = 83$ channels in this work) releasing an intensity matrix $\mathbf{I}_{\tau f}$ whose size is $N_{\tau} \times N_f$. In the second step, a preprocessing of $\mathbf{I}_{\tau f}$ is performed by multiplying $\mathbf{I}_{\tau f}$ with a masking matrix $\mathbf{M}_{f\theta}$, by which each frequency component in each τ section is mapped into N_{θ} virtual nodes (=400 in this work) releasing $\mathbf{P}_{\tau\theta}$. $\mathbf{M}_{f\theta}$ is a $N_f \times N_{\theta}$ matrix whose components are randomly selected among 0, 0.41, and 0.59 with a little higher possibility of taking 0 [61]. In the third step, each τ section in $\mathbf{P}_{\tau\theta}$ is sequentially concatenated releasing a time series, where each component in $\mathbf{P}_{\tau\theta}$ has a constant amplitude for a duration of θ . Since the value of θ sets the interaction strength between virtual nodes [61], it should be optimized and is set to 400 ns in this work. The obtained time series of the preprocessed signal multiplied by an appropriate voltage gain is applied to the OTS-based neuron device by using an arbitrary function generator (Tektronix AFG-3101) and the response of our neuron device is recorded by an oscilloscope (Tektronix TDS-5104). In the final step, the time series of the recorded response is converted into

a response matrix ($\mathbf{O}_{\tau\theta}$) with the same size as $\mathbf{P}_{\tau\theta}$ and is multiplied by a synaptic weight matrix $\mathbf{W}_{\theta i}$ giving a classifying matrix $\mathbf{Y}_{\tau i}$. Here, the subscript i indicates a class index corresponding to digits (0–9, integer). For training a word, $\mathbf{Y}_{\tau i}$ is given by the following rule: 1 for the right answer and 0 otherwise for all τ sections. And using $\mathbf{O}_{\tau\theta}$ and $\mathbf{Y}_{\tau i}$, is calculated by $\mathbf{W}_{\theta i} = (\mathbf{O}_{\tau\theta})^{\dagger} \mathbf{Y}_{\tau i}$, where $(\mathbf{O}_{\tau\theta})^{\dagger}$ is the Moore-Penrose pseudoinverse matrix of $\mathbf{O}_{\tau\theta}$. For the recognition test, $\mathbf{Y}_{\tau i}$ is calculated using the obtained $\mathbf{W}_{\theta i}$ and $\mathbf{O}_{\tau\theta}$ by $\mathbf{Y}_{\tau i} = \mathbf{O}_{\tau\theta} \times \mathbf{W}_{\theta i}$ and the maximum of the average of $\mathbf{Y}_{\tau i}$ over τ sections gives the guess. For this implementation, we compose a software using LabViewTM (National Instruments), whose processing speeds are about 3–4 words/s for training and 20–30 words/s for test in this work.

Figure 6(b) shows the result of the spoken-digit recognition test, where 450 voice files (ten digits \times nine utterances \times five females) are used for training and the remaining 50 voice files are used for test. The colormap shows the measure of probability ($\langle Y_{\tau i} \rangle_{\tau}$) as a function of the input spoken digit (j) and the class index ($i = 0-9$, integer), where i is the digit index for classifying an output. In order to distinguish five input voice files speaking the same digit (j), the j values are shifted in order by 0.2. For example, all $j \in [7.0, 7.2, 7.4, 7.6, 7.8]$ in Fig. 6(b) indicate the same spoken-digit “seven,” but are generated by five different persons. A correlation of $i \approx j$ is clearly seen rendering a high recognition accuracy (94%). We also perform the same test for all ten cases selecting nine utterances for training to find the average recognition accuracy of 85.4%.

These results clearly demonstrate that our OTS-based neuron device is highly promising for the application in the neuromorphic devices.

IV. CONCLUSION

In summary, we demonstrate that an artificial neuron device composed of an OTS and a few passive electrical components can mimic the behaviors of a biological neuron such as IF, rate coding, SFA, and chaotic activity. In addition, it is shown that the OTS-based neuron device can achieve the energy efficiency of a human brain with the state-of-the-art technology and the deliberate design of the device parameters. And in the last section, we successfully perform a spoken-digit recognition task using our OTS-based neuron device resulting in a high degree of recognition accuracy. Based on the presented results in this paper, we believe that the OTS-based artificial neuron provides a viable pathway to developing a large-scale brain-inspired and low-power-consuming computing system.

ACKNOWLEDGMENTS

This work is supported by the Korea Institute of Science and Technology (KIST) through 2E30761 and by National Research Foundation program through NRF-2019M3F3A1A02072175. H. Ju is financially supported by National Research Foundation program, NRF-2017R1E1A1A01077484.

-
- [1] F. C. Williams and T. Kilburn, Electronic digital computers, *Nature* **162**, 487 (1948).
 - [2] M. Mahowald and R. Douglas, A silicon neuron, *Nature* **354**, 515 (1991).
 - [3] B. Yan, X. Cao, and H. Li, in Proceedings of the 55th Annual Design Automation Conference (ACM, San Francisco, California, 2018), p. 1.
 - [4] G. Indiveri, B. Linares-Barranco, T. Hamilton, A. van Schaik, R. Etienne-Cummings, T. Delbruck, S.-C. Liu, P. Dudek, P. Häfliger, S. Renaud, *et al.*, Neuromorphic silicon neuron circuits, *Front. Neurosci.* **5** (2011).
 - [5] G. Indiveri, Synaptic plasticity and spike-based computation in VLSI networks of integrate-and-fire neurons, *Neural Inf. Process.* **11**, 135 (2007).
 - [6] S. R. Ovshinsky, Reversible electrical switching phenomena in disordered structures, *Phys. Rev. Lett.* **21**, 1450 (1968).
 - [7] M. H. Cohen, H. Fritzsche, and S. R. Ovshinsky, Simple band model for amorphous semiconducting alloys, *Phys. Rev. Lett.* **22**, 1065 (1969).
 - [8] P. W. Anderson, Model for the electronic structure of amorphous semiconductors, *Phys. Rev. Lett.* **34**, 953 (1975).
 - [9] R. A. Street and N. F. Mott, States in the Gap in glassy semiconductors, *Phys. Rev. Lett.* **35**, 1293 (1975).
 - [10] D. Adler, H. Hensch, and S. Mott, The mechanism of threshold switching in amorphous alloys, *Rev. Mod. Phys.* **50**, 209 (1978).
 - [11] N. F. Mott, Conduction in non-crystalline systems, *Philos. Mag.* **24**, 911 (1971).
 - [12] D. Ielmini, Threshold switching mechanism by high-field energy gain in the hopping transport of chalcogenide glasses, *Phys. Rev. B* **78**, 035308 (2008).
 - [13] D. Ielmini and Y. Zhang, Analytical model for subthreshold conduction and threshold switching in chalcogenide-based memory devices, *J. Appl. Phys.* **102**, 054517 (2007).
 - [14] L. Jennifer, K. Daniel, S. Martin, W. Matthias, and L. Christophe, Investigation of defect states in the amorphous phase of phase change alloys GeTe and Ge₂Sb₂Te₅, *Phys. Status Solidi c* **7**, 852 (2010).
 - [15] S. Caravati, M. Bernasconi, T. D. Kühne, M. Krack, and M. Parrinello, Coexistence of tetrahedral- and octahedral-like sites in amorphous phase change materials, *Appl. Phys. Lett.* **91**, 171906 (2007).
 - [16] K. DerChang, S. Tang, I. V. Karpov, R. Dodge, B. Klehn, J. A. Kalb, J. Strand, A. Diaz, N. Leung, J. Wu, *et al.*, in Electron Devices Meeting (IEDM), 2009 IEEE International (2009), pp. 1.
 - [17] F. T. Hady, A. Foong, B. Veal, and D. Williams, Platform storage performance With 3D XPoint technology, *Proc. IEEE* **105**, 1822 (2017).
 - [18] S. O. Pearson and H. S. G. Anson, Demonstration of some electrical properties of neon-filled lamps, *Proc. Phys. Soc. Lond.* **34**, 175 (1921).
 - [19] S. O. Pearson and H. S. G. Anson, The neon tube as a means of producing intermittent currents, *Proc. Phys. Soc. Lond.* **34**, 204 (1921).
 - [20] D. Ielmini, D. Mantegazza, and A. L. Lacaita, Voltage-Controlled relaxation oscillations in phase-change memory devices, *IEEE Electron Device Lett.* **29**, 568 (2008).
 - [21] S. Lavizzari, D. Ielmini, and A. L. Lacaita, A New transient model for recovery and relaxation oscillations in phase-change memories, *IEEE Trans. Electron Devices* **57**, 1838 (2010).
 - [22] T. Tuma, A. Pantazi, M. Le Gallo, A. Sebastian, and E. Eleftheriou, Stochastic phase-change neurons, *Nat. Nanotechnol.* **11**, 693 (2016).
 - [23] K. Moon, E. Cha, J. Park, S. Gi, M. Chu, K. Baek, B. Lee, S. Oh, and H. Hwang, in 2015 IEEE International Electron Devices Meeting (IEDM 2015), pp. 17.6.1.
 - [24] P. Stolar, J. Tranchant, B. Corraze, E. Janod, M.-P. Besland, F. Tesler, M. Rozenberg, and L. Cario, A leaky-integrate-and-fire neuron analog realized with a mott insulator, *Adv. Funct. Mater.* **27**, 1604740 (2017).
 - [25] S. Kumar, J. P. Strachan, and R. S. Williams, Chaotic dynamics in nanoscale NbO₂ mott memristors for analogue computing, *Nature* **548**, 318 (2017).
 - [26] W. Yi, K. K. Tsang, S. K. Lam, X. Bai, J. A. Crowell, and E. A. Flores, Biological plausibility and stochasticity in scalable VO₂ active memristor neurons, *Nat. Commun.* **9**, 4661 (2018).
 - [27] F. J. Morin, Oxides which show a metal-to-insulator transition at the neel temperature, *Phys. Rev. Lett.* **3**, 34 (1959).
 - [28] E. M. Izhikevich, Which model to use for cortical spiking neurons?, *IEEE Trans. Neural Networ.* **15**, 1063 (2004).

- [29] L. Chua, V. Sbitnev, and H. Kim, Neurons are poised near The edge of chaos, *Int. J. Bifurcation Chaos* **22**, 1250098 (2012).
- [30] J. Seiffter and J. A. Reggia, Lambda and the edge of chaos in recurrent neural networks, *Artif. Life* **21**, 55 (2015).
- [31] J. P. Crutchfield, Between order and chaos, *Nat. Phys.* **8**, 17 (2011).
- [32] S.-D. Kim, H.-W. Ahn, S. Y. Shin, D. S. Jeong, S. H. Son, H. Lee, B.-K. Cheong, D. W. Shin, and S. Lee, Effect of Ge concentration in $GexSe_{1-x}$ chalcogenide glass on the electronic structures and the characteristics of ovonic threshold switching (OTS) devices, *ECS Solid State Lett.* **2**, Q75 (2013).
- [33] E. D. Adrian and Y. Zotterman, The impulses produced by sensory nerve-endings: Part II. The response of a single End-organ, *J. Physiol.* **61**, 151 (1926).
- [34] F. Gabbiani and H. G. Krapp, Spike-Frequency adaptation and intrinsic properties of an identified, looming-sensitive neuron, *J. Neurophysiol.* **96**, 2951 (2006).
- [35] X.-J. Wang, Calcium coding and adaptive temporal computation in cortical pyramidal neurons, *J. Neurophysiol.* **79**, 1549 (1998).
- [36] H. R. Chandrasekhar and U. Zwick, Raman scattering and infrared reflectivity in GeSe, *Solid State Commun.* **18**, 1509 (1976).
- [37] D. I. Siapkas, D. S. Kyriakos, and N. A. Economou, Polar optical phonons and dielectric dispersion of GeSe crystals, *Solid State Commun.* **19**, 765 (1976).
- [38] See Supplemental Material at <http://link.aps.org/supplemental/10.1103/PhysRevApplied.13.064056> for additional details, including the calculation of characteristic time constants, the dependence of the delay time on the switching count, the validation of a deterministic nonlinear system, and SPICE modeling.
- [39] S. Lee, D. S. Jeong, J.-H. Jeong, W. Zhe, Y.-W. Park, H.-W. Ahn, and B.-K. Cheong, A study on the temperature dependence of the threshold switching characteristics of $Ge_2Sb_2Te_5$, *Appl. Phys. Lett.* **96**, 023501 (2010).
- [40] S.-Y. Shin, J. M. Choi, J. Seo, H.-W. Ahn, Y. G. Choi, B.-K. Cheong, and S. Lee, The effect of doping Sb on the electronic structure and the device characteristics of ovonic threshold switches based on Ge-Se, *Sci. Rep.* **4**, 7099 (2014).
- [41] S. R. Ovshinsky and H. Fritzsche, Amorphous semiconductors for switching, memory, and imaging applications, *IEEE Trans. Electron Devices* **20**, 91 (1973).
- [42] R. R. Shanks, Ovonic threshold switching characteristics, *J. Non-Cryst. Solids* **2**, 504 (1970).
- [43] S. H. Lee and H. K. Henisch, Threshold switching in chalcogenide glass films, *Appl. Phys. Lett.* **22**, 230 (1973).
- [44] Z. Borisova, *Glassy Semiconductors* (Springer US, New York, United States, 2013).
- [45] H. D. I. Abarbanel, R. Brown, J. J. Sidorowich, and L. S. Tsimring, The analysis of observed chaotic data in physical systems, *Rev. Mod. Phys.* **65**, 1331 (1993).
- [46] H. Suzuki, J.-I. Imura, Y. Horio, and K. Aihara, Chaotic Boltzmann machines, *Sci. Rep.* **3**, 1610 (2013).
- [47] S. A. Kauffman, Requirements for evolvability in complex systems: Orderly dynamics and frozen components, *Phys. D* **42**, 135 (1990).
- [48] F. Conti, L. J. De Felice, and E. Wanke, Potassium and sodium ion current noise in the membrane of the squid giant axon, *J. Physiol.* **248**, 45 (1975).
- [49] H. M. Fishman, Relaxation spectra of potassium channel noise from squid axon membranes, *Proc. Natl. Acad. Sci. U. S. A.* **70**, 876 (1973).
- [50] H. Hayashi and S. Ishizuka, Chaotic responses of the hippocampal CA₃ region to a mossy fiber stimulation in vitro, *Brain Res.* **686**, 194 (1995).
- [51] H. Hayashi, S. Ishizuka, and K. Hirakawa, Instability of harmonic responses of onchidium pacemaker neuron, *J. Phys. Soc. Jpn.* **55**, 3272 (1986).
- [52] K. Aihara, T. Numajiri, G. Matsumoto, and M. Kotani, Structures of attractors in periodically forced neural oscillators, *Phys. Lett. A* **116**, 313 (1986).
- [53] K. Aihara, G. Matsumoto, and M. Ichikawa, An alternating periodic-chaotic sequence observed in neural oscillators, *Phys. Lett. A* **111**, 251 (1985).
- [54] G. Matsumoto, K. Aihara, Y. Hanyu, N. Takahashi, S. Yoshizawa, and J.-I. Nagumo, Chaos and phase locking in normal squid axons, *Phys. Lett. A* **123**, 162 (1987).
- [55] J. P. Eckmann, S. O. Kamphorst, and D. Ruelle, Recurrence plots of dynamical systems, *EPL* **4**, 973 (1987).
- [56] N. Marwan, M. Carmen Romano, M. Thiel, and J. Kurths, Recurrence plots for the analysis of complex systems, *Phys. Rep.* **438**, 237 (2007).
- [57] Y. Hirata and K. Aihara, Devaney's chaos on recurrence plots, *Phys. Rev. E* **82**, 036209 (2010).
- [58] R. Devaney, *An Introduction To Chaotic Dynamical Systems* (Westview Press, London, United States, 2008).
- [59] Y. Hirata, M. Oku, and K. Aihara, Chaos in neurons and its application: Perspective of chaos engineering, *Chaos* **22**, 047511 (2012).
- [60] K. J. Yoon, Y. Kim, and C. S. Hwang, What will come after V-NAND—vertical resistive switching memory?, *Adv. Electron. Mater.* **5**, 1800914 (2019).
- [61] L. Appeltant, M. C. Soriano, G. Van der Sande, J. Danckaert, S. Massar, J. Dambre, B. Schrauwen, C. R. Mirasso, and I. Fischer, Information processing using a single dynamical node as complex system, *Nat. Commun.* **2**, 468 (2011).
- [62] J. Torrejon, M. Riou, F. A. Araujo, S. Tsunegi, G. Khalsa, D. Querlioz, P. Bortolotti, V. Cros, K. Yakushiji, A. Fukushima *et al.*, Neuromorphic computing with nanoscale spintronic oscillators, *Nature* **547**, 428 (2017).
- [63] L. Larger, A. Baylón-Fuentes, R. Martinenghi, V. S. Udaltsov, Y. K. Chembo, and M. Jacquot, High-Speed photonic reservoir computing using a time-delay-based architecture: Million words per second classification, *Phys. Rev. X* **7**, 011015 (2017).
- [64] Texas Instruments. 46-Word Speaker-Dependent Isolated Word Corpus (TI-46), NIST Speech Disk 7-1.1, <http://catalog.ldc.upenn.edu/LDC93S9> (NIST, 1991).